Optical line broadening mechanisms in rare-earth doped oxide nanocrystals

A. Fossati, Diana Serrano, Shuping Liu, Alexandre Tallaire, Alban Ferrier, Philippe Goldner

Highlights

Optical line broadening mechanisms in rare-earth doped oxide nanocrystals

A. Fossati,D. Serrano,S. Liu,A. Tallaire,A. Ferrier,P. Goldner

- Homogeneous linewidths of Eu^{3+} doped Y_2O_3 nanoparticles investigated as a function of temperature, magnetic field, and post-processing.
- We perform a detailed analysis and modeling of dephasing mechanisms specific to nanostructures leading to the identification of two-level systems and electric noise as main line broadening contributions.
- Modeling shows consistency with a line narrowing due to a reduction in the number of charged vacancy-pair defects.

Optical line broadening mechanisms in rare-earth doped oxide nanocrystals[⋆,⋆⋆]

A. Fossati[a,1], D. Serrano[a,*], S. Liu[a,b], A. Tallaire[a], A. Ferrier[a,c] and P. Goldner[a]

[a]Chimie ParisTech, PSL University, CNRS, Institut de Recherche de Chimie Paris, Paris, F-75005, France
[b]Shenzhen Institute for Quantum Science and Engineering and Department of Physics, Southern University of Science and Technology, 1088 Xueyuan Avenue Shenzhen, 518055, China
[c]Sorbonne Universite, Faculte des Sciences et Ingenierie, UFR 933, Paris, F-75005, France

ARTICLE INFO

Keywords:
nanoparticles
rare-earth
optical homogeneous linewidth
quantum technologies

ABSTRACT

Rare-earth ions in nanocrystals are promising solid-state platforms for quantum light-matter interfaces, combining millisecond-long nuclear spin T_2 with kHz-range optical homogeneous linewidths. Coupled to optical micro-cavities these materials can enable scalable quantum processors, nanoscale quantum memories and single photon sources. Here, we report on optical dephasing in Eu^{3+}:Y_2O_3 nanocrystals of 100 nm diameter through photon echo and spectral hole burning techniques as a function of temperature and magnetic field. We identify two-level systems (TLS) and electric noise as major line broadening mechanisms below 2 K and demonstrate that material-processing strategies such as high-power oxygen plasma can partially counteract these effects. Through modeling we show that these results are compatible with a reduction in the number of oxygen vacancy pairs in the nanocrystals by the oxygen plasma processing. These pairs, even at very low concentrations (hundreds of ppb), appear detrimental to optical coherence due to their ability to generate fluctuating electric fields.

1. Introduction

The emergence of quantum technologies has led to an intensive search for solid-state platforms allowing for quantum-state storage and manipulation. Those include rare-earth ions in crystals which are very attractive due to their record-long optical and spin coherence lifetimes [1, 2, 3, 4], the high qubit density they can support [5], and their ability to enable quantum storage [6, 7] and quantum-state conversion between optical and radio-frequency/microwave domains [8, 9]. In addition, the coupling of rare-earth emitters to photonic structures or optical micro-cavities provides Purcell enhanced emission rates for the weak $4f$-$4f$ transitions. This has enabled the realization of optical quantum nondemolition measurements with a single rare-earth ion qubit [10] and dynamic control of Purcell enhanced rare-earth emissions at telecom wavelength [11]. While the availability of high-quality bulk rare-earth crystals was at the basis of earlier demonstrations [1, 2], approaches requiring Purcell enhancement rely on the nanostructuration [12, 13] or thinning out of bulk samples [14]. There is also an alternative approach, which is the direct synthesis of rare-earth materials at the nanoscale [15]. Methods for obtaining quantum-grade rare-earth nanoparticles have been developed, yielding optical and spin coherence lifetimes (T_2) up to 12 μs and 8 ms respectively for 400 nm Eu^{3+}:Y_2O_3 particles [16, 17]. Promising coherence properties were also observed in Pr^{3+}:Y_2O_3 nanocrystals, with 3 (1) μs and 680 (640) μs optical and spin T_2 in 400 (150) nm particles respectively. These results have opened important perspectives towards miniaturized quantum hardware, and for efficient coupling to small-mode-volume and high-Q optical micro-cavities [18].

While spin T_2 values in rare-earth nanocrystals are comparable to those observed in bulk materials [19, 17], the scope for improvement remains large in the optical domain where best obtained results are still about two orders of magnitude below reference bulk values [20]. Preserving long optical T_2 values is however of utmost importance for the performance of quantum protocols based on rare-earth ions [5, 6, 7]. Indeed, major progress could be attained by identifying the dominating dephasing mechanisms in these nanomaterials and finding solutions to counteract them during material fabrication. In particular, defect engineering was recently proposed to reduce optical dephasing in oxide nanoparticles [21]. In that work, it was shown that oxygen-related defects in Y_2O_3 could be modified under a pure oxygen plasma excited by a high-power microwave (MW) source leading to optical T_2 enhancement, i.e. homogeneous linewidth ($\Gamma_h = (\pi T_2)^{-1}$) narrowing. These long optical coherence lifetimes could be harnessed to demonstrate coherent electro-optical storage up to 40 μs [22].

In the present work, we thoroughly analyse the impact of oxygen plasma treatment on the different contributions to the optical homogeneous line Γ_h of Eu^{3+} in Y_2O_3, including spectral diffusion (SD), two-level systems (TLS), two-phonon processes, and broadening due to magnetic and electric noises. The study, performed on single crystalline Eu^{3+}:Y_2O_3 nanoparticles of 100 nm average size doped at 0.3% at., shows two major sources of line broadening below 2 K: TLS and electric noise. We show that these two contributions are significantly reduced after high-MW-power oxygen plasma processing and that spectral diffusion is also reduced. In addition, a model considering charge tunneling between first-neighbor oxygen vacancies is proposed to account for the observed electric noise contribution. We

diana.serrano@chimieparistech.psl.eu (D. Serrano)
ORCID(s):

Table 1
Spectroscopic properties of the investigated Eu^{3+}:Y_2O_3 nanoparticles. Γ_{inh} and T_1 were measured at 12 K and room temperature, respectively. T_2 values were obtained at 1.4 K.

Sample	Plasma treated	Untreated
Peak abs. (nm, vac.)	580.8830	580.8815
Γ_{inh} (GHz)	27	11
T_1 (ms)	1.43	1.35
T_2 (μs)	5.67±0.21	1.91±0.04

estimate a concentration of tunneling oxygen-vacancy pairs in the particles in the order of hundreds of ppb. This result also highlights the extreme sensitivity of rare-earths' optical transitions to material defects, thus their potential to be used as very sensitive defect probes.

The manuscript is organized as follows: experimental details and methods are given in Sec. 2. In Sec. 3.1 we describe the line broadening contributions to Γ_h. High-resolution spectroscopic results are given in Sec. 3.2, including two-pulse photon echoes as a function of magnetic field, and three-pulse echoes and Γ_h as a function of temperature. In Sec. 3.3, the major contributions to optical dephasing are discussed and the charge-tunneling model is proposed to account for the additional broadening in this nanomaterial. General conclusions are given in Sec. 4.

2. Experimental

The Eu^{3+}:Y_2O_3 nanoparticles used in this study were obtained from Eu^{3+} doped hydroxycarbonate amorphous nanoparticles (YOC) after annealing at 800 °C and 1200 °C for 18 h and 6 h respectively, as described in [21]. This yields a white powder composed of well-dispersed single-crystalline objects, with pure cubic phase (Ia-3 space group) and average particle diameter of 100 nm, confirmed by X-ray diffraction (XRD) and transmission electron microscopy (TEM). These structural and morphological characterizations can be found in a previous work [21]. The total Eu^{3+} concentration is 0.3% at., with the Eu^{3+} dopants replacing Y^{3+} lattice ions at sites with C_2 and C_{3i} point symmetry. In the following, only Eu^{3+} ions at C_2 sites are considered as the transition of interest, $^7F_0 \leftrightarrow {}^5D_0$, vanishes for Eu^{3+} ions occupying C_{3i} sites. A portion of the obtained powders was additionally processed under high-microwave-power pure oxygen plasma. The plasma duration was set to three minutes, and repeated twice. Spectroscopic properties of the $^7F_0 \leftrightarrow {}^5D_0$ transition in investigated samples, reported in a previous work [21], are given in Table 1.

For low-temperature spectroscopic investigations, 5 mg of oxygen plasma treated and 5 mg of untreated powders were put inside two separate containers of a home-built sample holder. The powders take the shape of the containers forming slabs of ~ 500 μm thickness. The different contributions to optical dephasing in oxygen plasma treated and untreated nanoparticles were investigated by photon echo and spectral hole burning (SHB) methods adapted to highly-scattering media [23, 24]. External magnetic fields up to 2.5 T and temperatures from 1.4 K to 20 K were used. Experiments requiring external magnetic field were carried out at 2.1 K in superfluid He, using a bath cryostat equipped with a superconducting magnet. All other experiments were performed in a Janis SVT-200 He bath cryostat operated in gas mode. Temperature was regulated by tuning the He gas pressure for T < 6 K, while the built-in heating system was used for temperatures above 6 K. A Si diode (Lakeshore DT-670) attached to the sample container was used for monitoring temperature.

Photon echo and SHB pulse sequences were created by shaping and frequency-shifting the CW output at ≈ 581 nm (see Table 1) of a frequency-stabilized dye laser (Sirah Matisse DS - 250 kHz linewidth), with an acousto-optic modulator (AOM - AA Opto Electronic MT200) driven by an arbitrary waveform generator (Agilent N8242A). The laser pulses were focused on the powder samples using a 75 mm lens, and light transmitted and emitted by the samples was focused on an avalanche photodiode (Thorlabs APD110A) for detection. Echo signals from two-pulse and three-pulse echo sequences were detected through their beating with a frequency-shifted pulse with 30 MHz detuning. The decay of the echo amplitude was recorded as a function of the $\pi/2$ and π pulses separation in two-pulse echo measurements, and as a function of the separation between the two first $\pi/2$ pulses for a fixed waiting time T_W between the last two $\pi/2$ pulses, in three-pulse echo measurements. T_2 values were extracted from echo decay curves by single exponential or stretched exponential fits when decays did not show single-exponential character (e.g. longest waiting times in Figure 2).

Pulse lengths and intensities were optimized to obtain echo signals with maximum signal-to-noise ratio (SNR). In particular, 200 mW incident power was used for π pulses of 1.5 μs duration. The SNR was further improved by echo signal averaging over 100 shots.

Spectral holes in the $^7F_0 \leftrightarrow {}^5D_0$ transition were created by optically pumping for 1 ms with 50 mW incident power, and probed by a 15 mW scanning pulse with a scan rate of 100 MHz ms^{-1}. Such high readout power was used due to the small fraction ($\sim 10^{-5}$) of the incident intensity transmitted through the strongly scattering powder samples [24]. The waiting time between burning and readout pulses was set to 2 ms. A band-pass filter with a transmission window of 10 nm, centered around 580 nm (Thorlabs FB580-10) was used in all sequences for fitering out the strong Eu^{3+} $^5D_0 \rightarrow {}^7F_2$ fluorescence at 611 nm.

3. Results and discussion

3.1. Theory

The optical homogeneous linewidth Γ_h results from addition of several contributions expressed as:

$$\Gamma_h = \Gamma_{pop} + \Gamma_{ion} + \Gamma_{spin} + \Gamma_{ph} + \Gamma_{TLS} + \Gamma_{e^-} \qquad (1)$$

where $\Gamma_{pop}=(2\pi T_1)^{-1}$ is the natural linewidth due to the excited-state population lifetime, constituting the absolute

lower limit to Γ_h. All other terms in Eq. 1 result from interactions between the Eu^{3+} ions and the environment.

Among different types of interactions we distinguish (i) the excitation-induced interaction between active ions (Γ_{ion}), proportional to the concentration of excited ions (N_{exc}), and leading to the phenomenon of instantaneous spectral diffusion (ISD) [25]; (ii) the interaction between active Eu^{3+} ions and surrounding electron and nuclear spins from host lattice ions, other dopant ions, and magnetic defects (Γ_{spin}); (iii) interactions with lattice phonons (Γ_{ph}), which in the Eu^{3+} case exhibit a T^7 temperature dependence corresponding to elastic Raman scattering [26]; (iv) perturbations due to tunneling between nearly equivalent configurations, also known as two-level systems (TLS) and presenting linear or quasi-linear dependence with temperature [27]; and (v) electric interaction with free electrons, charged defects and dangling bonds (Γ_{e^-}) [23, 28]. The last two terms, Γ_{TLS} and Γ_{e^-}, are often neglected in bulk rare-earth crystals [29, 30] while they are relevant contributions to the optical linewidth in rare-earth doped ceramics and nanoparticles [23, 31, 32].

3.2. Experimental results

3.2.1. *Magnetic field dependence of* Γ_h

Treating Y_2O_3 nanoparticles with high-MW-power pure oxygen plasma leads to a neat reduction in optical dephasing. This has been reported for several rare-earth ions, and for nanoparticles presenting different sizes [16, 19, 21]. In the present case, T_2 measured by two-pulse photon echoes for the $^7F_0 \leftrightarrow {}^5D_0$ transition at zero magnetic field increases from 1.91 ± 0.04 μs for the untreated sample (Fig. 1 green curve) to 5.7 ± 0.2 μs after treatment (Fig. 1 red curve). This corresponds to a homogeneous linewidth reduction of more than 100 kHz, from 167 ± 7 kHz to 56 ± 4 kHz. Signals corresponding to electrons trapped at oxygen vacancies (F^+ centers) and O_2^- interstitial defects were observed in Eu^{3+}:Y_2O_3 nanoparticles treated with oxygen plasma by electron paramagnetic resonance (EPR) investigations [21]. These paramagnetic defects can induce additional broadening through local magnetic field fluctuations produced by their relaxation and flip-flop dynamics. Modeled as unpaired electrons with g=2, they present a Zeeman splitting of the order of $\mu_B g$ = 28 GHz T^{-1}, where μ_B = 14 GHz T^{-1}. At 2.1 K and under 2.5 T of external magnetic field, 80% of these defects get polarized to their lower energy state, which reduces magnetic noise. Optical T_2 values measured at 2.1 K under external magnetic fields from zero to 2.5 T are displayed in the inset of Fig. 1. No T_2 increase is observed when increasing magnetic field intensity for untreated (green dots) or treated (red dots) nanoparticles. This lack of a magnetic field dependence indicates either that the concentration of these impurities is too low to have an impact, or that the added dephasing due to these species is negligible on the T_2 time scale (2-4 μs at 2 K). The latter is indeed quite likely as Γ_h increase due to the interaction with electrons trapped in oxygen vacancies was estimated at 2 kHz in Eu^{3+}:Y_2O_3 transparent ceramics [33], a very low value compared to the

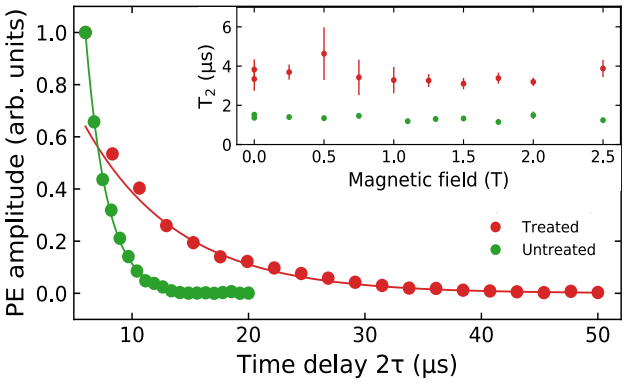

Figure 1: Photon echo decay curves from oxygen plasma treated (red) and untreated (green) nanoparticles measured at T = 1.4 K and B = 0 T. T_2 values of 5.7 ± 0.2 μs and 1.91 ± 0.04 μs were obtained by exponential fit to the experimental data (solid lines). The excitation wavelength was set to the maximum absorption wavelength for each sample (Table 1). Inset: Optical T_2 as a function of external magnetic field in oxygen plasma treated (red) and untreated (green) nanoparticles measured at T = 2.1 K.

84 kHz (174 kHz) homogeneous linewidths derived from T_2 values in Fig. 1, inset, for treated (untreated) nanoparticles.

3.2.2. *Spectral diffusion*

Time-dependent broadening in the nanoparticles was assessed by three-pulse photon echoes, also referred to as stimulated echoes. Those could be detected up to a few ms in the oxygen plasma treated nanoparticles (Fig. 2(a)). Instead, rapid worsening of the signal to noise ratio was observed when increasing the waiting time (T_W) in the untreated sample preventing measurements beyond 500 μs of delay (Fig. 2(b)). Both samples showed time-dependent broadening although the amount of spectral diffusion was significantly larger for the untreated sample, with 300 kHz of added dephasing in 100 μs. This is reduced to 100 kHz in 1 ms by the treatment. Data in Fig. 2(b) were modeled using the sudden-jump spectral diffusion (SD) model:

$$\Gamma_{\mathrm{eff}}(T_W, \tau) = \Gamma_0^{\mathrm{SD}} + \frac{1}{2}\Gamma_{\mathrm{SD}}[1 - \exp(-RT_W)] \qquad (2)$$

where Γ_{eff} is the effective homogeneous linewidth including spectral diffusion, R is the flip rate of the perturbating species, Γ_0^{SD} the linewidth without spectral diffusion, and Γ_{SD} the spectral diffusion linewidth. Best-fit parameter values to experimental data points in Figure 2 are given in Table 2 together with SD parameters from 400 nm Y_2O_3 nanoparticles [23]. SD-free Γ_0^{SD} values are slightly larger, about 20%, than Γ_h values measured by two-pulse photon echoes (Fig. 1), which we attribute to fluctuations of the experimental conditions between measurements. Data in Fig. 2(a) is not sufficient for a good estimation of R and Γ_{SD} parameters in the oxygen plasma treated sample as the characteristic plateau of SD curves is not reached in

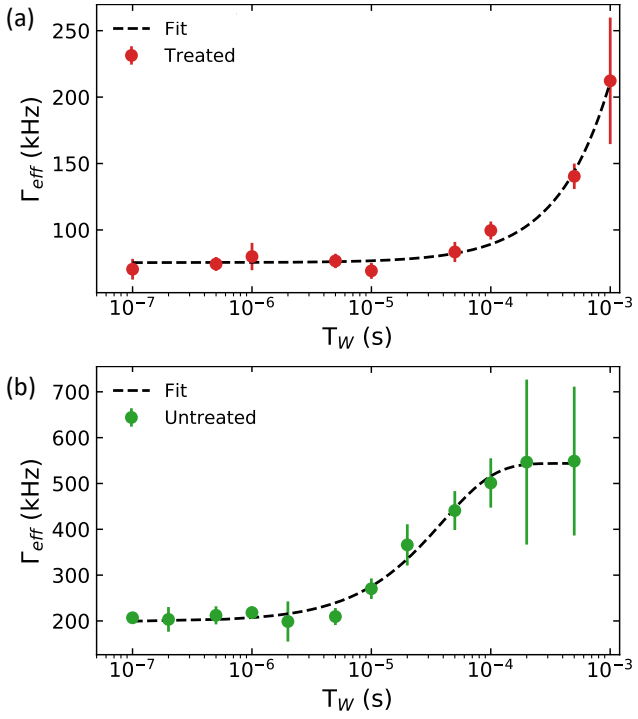

Figure 2: (a) Optical homogeneous linewidth as a function of waiting time T_W in oxygen plasma treated (a) and untreated (b) nanoparticles. Dotted lines are fitted curves using Eq. 2 and parameters in Table 2. T = 1.4 K for all measurements.

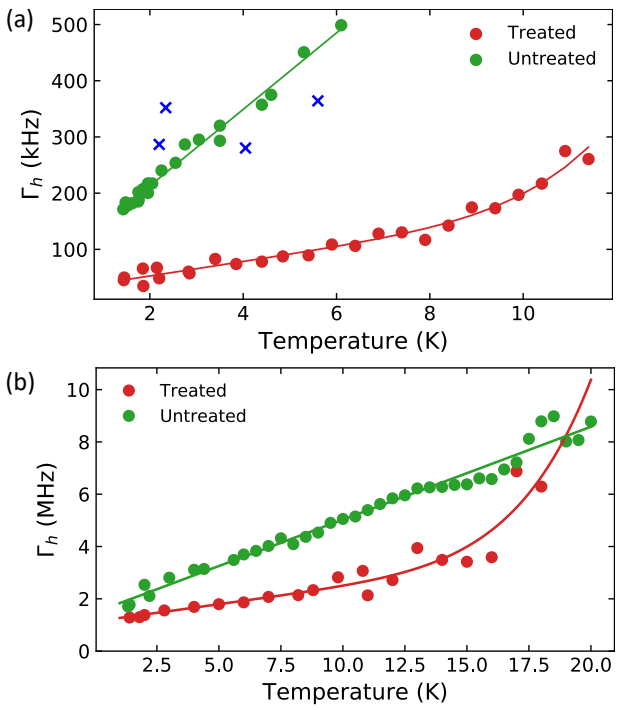

Figure 3: (a) Optical homogeneous linewidth as a function of temperature in oxygen plasma treated (red) and untreated (green) nanoparticles obtained from two-pulse photon echoes. Blue crosses indicate experimental points not taken into account for the fit and are attributed to temperature instabilities during measurements due to He gas flow fluctuations. (b) Optical homogeneous linewidth derived from spectral hole widths as $\Gamma_h = (\Gamma_{hole}\text{-}\Gamma_{laser})/2$, as a function of temperature in oxygen plasma treated (red) and untreated (green) nanoparticles.

Table 2
Spectral diffusion parameters Γ_0^{SD}, Γ_{SD} and R for Eu^{3+}:Y_2O_3 nanoparticles.

Sample	Γ_0^{SD} (kHz)	Γ_{SD} (kHz)	R (kHz)
100 nm treated	75±2	~ 1100	~ 0.3
100 nm untreated	198±7	690±26	25±3
400 nm untreated [23]	90	380	0.8

the investigated T_W range. Still, the rapid Γ_{eff} increase for waiting times $T_W > 100$ μs shows quite good agreement with R of the order of 300 Hz and Γ_{SD} of ~1.1 MHz (Table 2). In contrast, much larger R is found before treatment, equal to 25 kHz (Table 2). This is between one and two orders of magnitude larger than R values reported in 400-nm Eu^{3+}:Y_2O_3 nanoparticles (Table 2) and ceramics [23, 34]. It reveals the presence of a faster-dynamics defect that appears cured, or at least slowed down, by the oxygen plasma treatment.

3.2.3. Temperature dependence of Γ_h

Relevant information about optical dephasing mechanisms in rare-earth crystals is often obtained from the temperature dependence of the homogeneous linewidths [30, 33]. Γ_h as a function of temperature is shown in Fig. 3(a) for oxygen plasma treated and untreated nanoparticles. These Γ_h values were derived from optical T_2 decays obtained by two-pulse photon echoes. The untreated sample (green dots) shows a linear trend with temperature, scaling as 68 kHz K^{-1}. This linear behaviour, previously observed in Eu^{3+}:Y_2O_3 nanoparticles [23], transparent ceramics [31] and some bulk rare-earth crystals [35], is attributed to local disorder modes, also known as tunneling two-level systems (TLS). Up to 8 K, oxygen plasma treated nanoparticles also show a linear temperature-dependent broadening (Fig. 3(a)) although with a lower slope of 13 kHz K^{-1}. For temperatures higher than 8 K, Γ_h increases as T^7, consistent with two-phonon Raman scattering processes [30].

A larger temperature range is accessible through spectral hole burning measurements (Fig. 3(b)). In those experiments, Γ_h can be estimated as $(\Gamma_{hole}\text{-}\Gamma_{laser})/2$, where Γ_{hole} is the full width at half maximum (FWHM) of the measured spectral hole and Γ_{laser} the laser linewidth contribution. SHB is not suitable for characterizing narrow Γ_h, as the narrowest holes which can be measured are ultimately limited by the laser linewidth. In contrast, it is convenient for exploring higher temperatures, where Γ_h gets broad and T_2 becomes too short to be measured by two-pulse echoes. The temperature trends observed in Fig. 3(a) are confirmed and extended to higher temperatures by the SHB measurements: Γ_h is dominated by linear TLS broadening up to 20 K in untreated nanoparticles (Fig. 3(b), green dots) while the treatment reduces the TLS slope. Interestingly, this disorder reduction

Table 3
Γ_0^T, α_{TLS} and α_{TPR} parameters obtained by two-pulse photon echo (2PPE) and/or SHB measurements, in Eu^{3+}:Y_2O_3 nanoparticles.

Sample	Γ_0^T (kHz)	α_{TLS} (kHz K^{-1})	α_{TPR} (kHz K^{-7})
100 nm treated			
2PPE	27±6	13±1	$(4\pm1)\cdot10^{-6}$
SHB	1100±200	132±34	$(10\pm2)\cdot10^{-6}$
100 nm untreated			
2PPE	77±5	68±2	-
SHB	1500±100	355±9	-
400 nm treated [23]			
2PPE/*SHB	45±10	9±1	$^{*}(5\pm1)\cdot10^{-6}$

occurs even though a larger inhomogeneous linewidth is measured in the treated sample (Table 1), indicating that the increased inhomogeneity has no detrimental impact on Γ_h and highlighting the absence of correlation between static and dynamic broadening. The usual T^7 broadening is also observed in the treated sample for T > 15 K (Fig. 3(b), red dots). $\Gamma_h(T)$ curves in Fig. 3 were fitted by:

$$\Gamma_h(T) = \Gamma_0^T + \alpha_{TLS} T + \alpha_{TPR} T^7 \quad (3)$$

where α_{TLS} is the TLS coupling constant, α_{TPR} the two-phonon Raman coupling constant and Γ_0^T is the limit at 0 K, representing the temperature-independent broadening contributions. Best-fit parameters to Eq. 3 are given in Table 3. While trends are similar and both sets of data show clear reduction of TLS dephasing by the oxygen plasma treatment, there is a discrepancy between Γ_h values measured by photon echoes and SHB methods. This can be partly explained by the difference in time scale at which Γ_h is probed using these two techniques: a few μs in the photon echo case, and several ms in the SHB one. Therefore, at the ms time scale, we know from three pulse echo measurements that additional broadening, of at least several hundreds of kHz, is expected due to spectral diffusion (Fig. 2). In addition, holes can be further broadened because of long term laser instabilities, temperature fluctuations in the cryostat and power broadening [23]. An interesting point is the significant increase in α_{TLS} observed in SHB measurements compared to photon echo ones (Table 3). This may indicate a stronger TLS coupling at longer times which can be due to a higher TLS density of states related to the added contribution from slower TLS at longer times. In contrast, similar α_{TPR} is found in Fig. 3(a) and Fig. 3(b) for oxygen plasma treated nanoparticles (Table 3). Finally, both echo and SHB measurements confirm a reduction of the temperature independent broadening (Γ_0^T) by the oxygen plasma treatment.

3.3. Discussion

This study shows that the oxygen plasma processing has a clear impact on several of the dephasing contributions

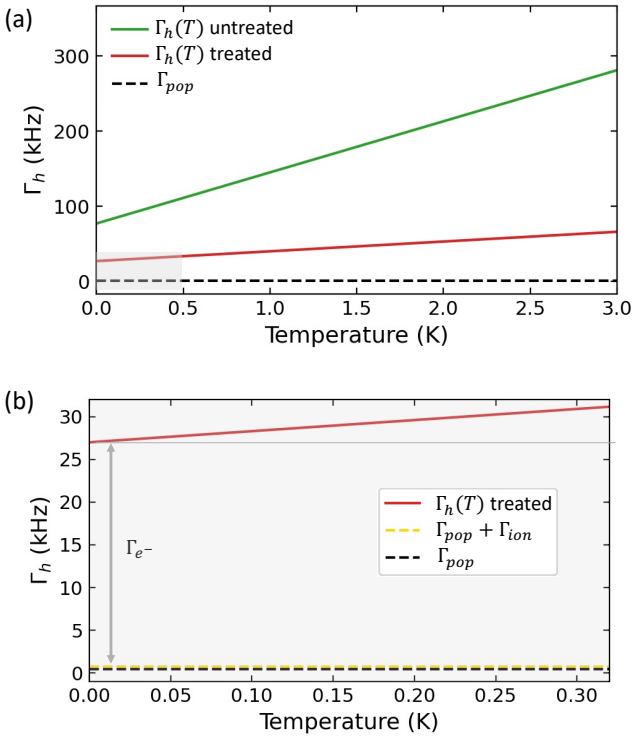

Figure 4: (a) Simulated optical homogeneous broadening as a function of temperature using Eq. 3 and best-fit parameters from Table 3 for untreated (green) and treated (red) nanoparticles. The dotted line represents Γ_{pop}, i.e. the population lifetime limited linewidth. (b) Zoom between 0 and 0.32 K where the difference between Γ_h and $\Gamma_{pop}+\Gamma_{ion}$ (yellow dotted line) is attributed to temperature-independent electric noise.

in Equation 1: it lowers down spectral diffusion (Figure 2) and significantly reduces TLS dephasing (Figure 3), which accounts for 90 kHz at 1.4 K in the untreated nanoparticles while for only 29 kHz in the treated ones. It also decreases the temperature-independent linewidth (Γ_0^T) by a factor of three (Figure 4(a)). We attribute the lower bound linewidth Γ_0^T to electric dephasing ($\Gamma_{e^-} \sim \Gamma_0^T$) as the lack of magnetic field dependence (Figure 1 inset) allows discarding magnetic noise from paramagnetic defects, and Γ_{pop} and Γ_{ion} are negligible compared to Γ_0^T (Figure 4(b)). More into details, Γ_{pop} equals 111 (117) Hz in treated (untreated) nanoparticles, determined as $(2\pi T_1)^{-1}$ (Table 1). Γ_{ion} due to ISD is also very small, estimated at 500 Hz for the untreated sample, and reduced to 230 Hz after oxygen plasma treatment (see [21] for details). This reduction is attributed to the increased inhomogeneous linewidth (Table 1), which translates into a reduction of number of excited ions for equal excitation bandwidth.

Electric noise was previously suggested as a relevant line broadening mechanism in rare-earth nanoparticles below 2 K. This was tentatively attributed to a fluctuating surface charge density in a previous work [23]. Here, we report a threefold reduction of the temperature-independent

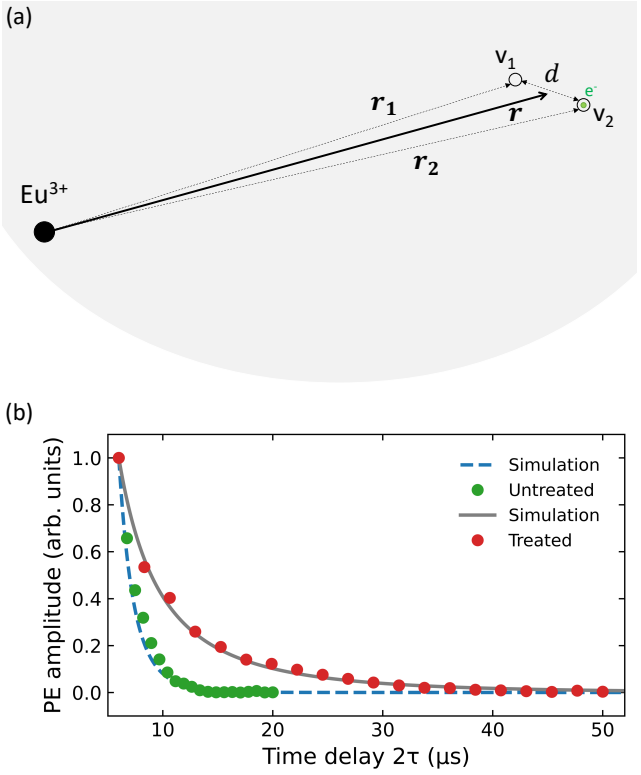

Figure 5: (a) Schematic representation of a pair of oxygen vacancies separated by a distance d and at a distance r from an Eu^{3+} ion. A fluctuating electric field $\delta\mathbf{E}(\mathbf{r}) = \mathbf{E}(\mathbf{r_1}))-\mathbf{E}(\mathbf{r_2})$ at the Eu^{3+} position is generated by an electron tunneling between the two vacancies. We consider $d << r$, thus $r \sim r_1 \sim r_2$. (b) Simulated photon echo decays using Eq. 6 compared to experimental ones. Best agreement was obtained for defect concentrations of 140 ppb (dashed blue line) and 570 ppb (solid gray line) for treated and untreated nanoparticles respectively.

linewidth dominated by Γ_{e^-} after the oxygen plasma treatment. However, there is no evidence of modification of the nanoparticles surface by the latter [21]. In contrast, the oxygen plasma processing was shown to quantitatively modify the amounts of oxygen-related defects in the Y_2O_3 particles volume, reducing neutral and charged oxygen vacancies while increasing interstitial oxygen. This suggests that these defects can be a non-negligible source of electric noise in this material as oxygen vacancies can be found in different charge states in Y_2O_3, from neutral to 2+ [36]. Charge trapping and charge tunneling between neighboring oxygen vacancies could therefore be a source of fluctuating electric field within the material. The frequency shift of Eu^{3+} optical transition due to an external electric field can be expressed as:

$$\Gamma_{\text{Stark}} = \mathbf{S} \cdot \mathbf{E}(\mathbf{r}) \tag{4}$$

where $\mathbf{E}(\mathbf{r})$ is the external electric field and $\mathbf{S}$ the Stark coefficient, measured at 480 Hz/(V/m) for the $^7F_0 \leftrightarrow {}^5D_0$ transition in Y_2O_3 [22]. If we now consider a single electron tunneling between two first-neighbor oxygen vacancies separated by a distance d, and at distances $\mathbf{r_1}$ and $\mathbf{r_2}$ from an Eu^{3+} ion respectively (Figure. 5(a)), the electric broadening Γ_{e^-} can be expressed as $\Delta\Gamma_{\text{Stark}} = \mathbf{S} \cdot \delta\mathbf{E}(\mathbf{r})$ where $\delta\mathbf{E}(\mathbf{r}) = \mathbf{E}(\mathbf{r_1}) - \mathbf{E}(\mathbf{r_2})$. For $d << r_1, r_2$, $\delta\mathbf{E}(\mathbf{r})$ can be approximated as:

$$\delta\mathbf{E}(\mathbf{r}) = -\frac{q}{4\pi\epsilon_0 k}\frac{2\mathbf{\Delta r}}{r^3} \tag{5}$$

with $r \sim r_1 \sim r_2$ the distance between the ion and the vacancy-pair defect, q = 1.602 10^{-19} C the electron charge, k the dielectric constant for bulk Y_2O_3, equal to 15, and $\mathbf{\Delta r} = \mathbf{r_1} - \mathbf{r_2}$.

To model the optical line broadening due to these defects, the decay of the photon echo amplitude as a function of time delay 2τ was simulated as:

$$A_{echo}(\tau) = \sum_{i=1}^{N} \exp(-2\pi\tau\Delta\Gamma_{\text{Stark,i}}) \tag{6}$$

where $\Delta\Gamma_{\text{Stark,i}}$ is the linewidth of the i^{th} Eu^{3+} ion contributing to the echo signal. Using a Monte Carlo approach, every $\Delta\Gamma_{\text{Stark,i}}$ was estimated by randomly placing a number of randomly-oriented vacancy-pair defects in the particle volume, then calculating the broadening induced by each of these defect on an Eu^{3+} ion placed at the center of the particle by using Eq. 5, and finally selecting the larger broadening value. The distance d between the two vacancies was set at 3.2 Å, equal to the maximum distance separating first-neighbor oxygen ions in Y_2O_3 [37]. The simulation was completed by repeating the previous steps for $5{\times}10^4$ times, equivalent to evaluating contributions from $5{\times}10^4$ Eu^{3+} ions. The number of defects per particle was the only adjustable parameter and was determined by best-fit to the experimental data in Fig. 1. As displayed in Figure. 5(b), quite good agreement is obtained for a vacancy-pair defect concentration of 140 ppb (570 ppb) in treated (untreated) particles. We note that the total number of excited Eu^{3+} ions per particle is estimated at 1.3 by considering the Eu^{3+} concentration in the nanoparticles and ratio between excitation bandwidth (~1 MHz) and inhomogeneous broadening, and that the previously mentioned defect concentrations correspond to just 3 (12) defects per particle. We therefore discard the possibility for the same defect to be the dominating dephasing source for two different Eu^{3+} ions.

While the estimated defect concentrations are very low in both samples, the modeling shows that they are still sufficient to broaden Γ_h to several tens of kHz, and that reduction by a factor of four of these type of detrimental defects can significantly reduce Γ_h. Oxygen vacancy defects in Y_2O_3 have been also linked to increased disorder and TLS dephasing [38]. This is consistent with the larger TLS contribution to dephasing in untreated nanoparticles together with the larger defect concentration derived from the modeling. On the other hand, the very low concentration values of 140 ppb and 570 ppb for treated and untreated nanoparticles respectively, could explain the absence of magnetic field dependence. Ultimately, we show here that narrow homogeneous linewidths in nanocrystals constitute an extremely

sensitive probe for charged material defects, and demonstrate that material processing techniques offer resources for counteracting detrimental dephasing mechanisms leading to improved optical coherence properties.

4. Conclusion

In this manuscript we investigate the homogeneous linewidth of Eu^{3+}:Y_2O_3 nanoparticles of 100 nm as a function of magnetic field, delay time and temperature. From the experimental results we conclude that two-level systems and electric noise are the major contributions to Γ_h below 2 K and that those contributions can be significantly reduced by material processing, in the present case, by high-power oxygen plasma. Finally, we correlate the spectroscopic results with the material properties using a simple model based on electric noise from material defects, in particular, charged oxygen vacancy pairs, consistent with the observed Γ_h values in rare-earth doped Y_2O_3 nanoparticles. From the modeling we estimate the concentration of these defects at 140 ppb (570 ppb) in treated (untreated) nanoparticles, attributing the narrower temperature-independent linewidth in treated nanoparticles to a reduction in defect content of a factor four. These results confirm the potential of these nanomaterials for quantum processing as the measured Γ_h in treated nanoparticles is narrow enough to spectrally resolve $\Gamma_{inh}/\Gamma_h \sim 10^5$ Eu^{3+} qubits. Besides, the linewidth is also narrow enough to reveal interactions in the 10s of kHz range. This could be harnessed for sensing purposes, and in particular to probe small amounts of materials defects undetectable by standard characterization techniques.

5. Acknowledgements

This project has received funding from the European Union Horizon 2020 research and innovation program under grant agreement no. 712721 (NanOQTech) and no. 820391 (SQUARE), from the French Agence Nationale de la Recherche under grant ANR-20-CE09-0022-01 (UltraNanOSpec) and from the Science and Engineering Network of Ile de France for Quantum Technologies (SIRTEQ). S. Liu is supported by the Key R&D Program of Guangdong province (Grant No. 2018B030325001) and Guangdong Basic and Applied Basic Research Foundation (No. 2021A1515110191).

References

[1] M. Zhong, M. P. Hedges, R. L. Ahlefeldt, J. G. Bartholomew, S. E. Beavan, S. M. Wittig, J. J. Longdell, M. J. Sellars, Optically addressable nuclear spins in a solid with a six-hour coherence time, Nature 517 (2015).

[2] M. Rancic, M. P. Hedges, R. L. Ahlefeldt, M. J. Sellars, Coherence time of over a second in a telecom-compatible quantum memory storage material, Nat. Physics (2017) 4254.

[3] T. Böttger, C. W. Thiel, Y. Sun, R. L. Cone, Optical decoherence and spectral diffusion at 1.5 μm in Er^{3+}:Y_2SiO_5 versus magnetic field, temperature, and er^{3+} concentration, Physical Review B 73 (2006) 075101.

[4] S. Welinski, A. Tiranov, M. Businger, A. Ferrier, M. Afzelius, P. Goldner, Coherence Time Extension by Large-Scale Optical Spin Polarization in a Rare-Earth Doped Crystal, Physical Review X 10 (2020) 031060. Publisher: American Physical Society.

[5] A. Kinos, D. Hunger, R. Kolesov, K. Mølmer, H. de Riedmatten, P. Goldner, A. Tallaire, L. Morvan, P. Berger, S. Welinski, K. Karrai, L. Rippe, S. Kröll, A. Walther, Roadmap for Rare-earth Quantum Computing, arXiv:2103.15743 [quant-ph] (2021). ArXiv: 2103.15743.

[6] A. Ortu, A. Holzäpfel, J. Etesse, M. Afzelius, Storage of photonic time-bin qubits for up to 20 ms in a rare-earth doped crystal, npj Quantum Information 8 (2022) 1–7.

[7] D. Lago-Rivera, S. Grandi, J. V. Rakonjac, A. Seri, H. de Riedmatten, Telecom-heralded entanglement between multimode solid-state quantum memories, Nature 594 (2021) 37–40.

[8] P. S. Barnett, J. J. Longdell, Theory of microwave-optical conversion using rare-earth-ion dopants, Physical Review A 102 (2020) 063718.

[9] J. G. Bartholomew, J. Rochman, T. Xie, J. M. Kindem, A. Ruskuc, I. Craiciu, M. Lei, A. Faraon, On-chip coherent microwave-to-optical transduction mediated by ytterbium in YVO4, Nature Communications 11 (2020) 3266.

[10] M. Raha, S. Chen, C. Phenicie, M. S. Ourari, A. M. Dibos, J. D. Thompson, Optical quantum nondemolition measurement of a single rare earth ion qubit, Nature Communications 11 (2020).

[11] B. Casabone, C. Deshmukh, S. Liu, D. Serrano, A. Ferrier, T. HÃŒmmer, P. Goldner, D. Hunger, H. de Riedmatten, Dynamic control of Purcell enhanced emission of erbium ions in nanoparticles, Nature Communications 12 (2021).

[12] T. Zhong, J. Rochman, J. M. Kindem, E. Miyazono, A. Faraon, High quality factor nanophotonic resonators in bulk rare-earth doped crystals, Optics Express 24 (2016) 536–544.

[13] A. M. Dibos, M. Raha, C. M. Phenicie, J. D. Thompson, Atomic source of single photons in the telecom band, Phys. Rev. Lett. 120 (2018) 243601.

[14] B. Merkel, A. Ulanowski, A. Reiserer, Coherent and Purcell-Enhanced Emission from Erbium Dopants in a Cryogenic High-Q Resonator, Physical Review X 10 (2020) 041025. Publisher: American Physical Society.

[15] T. Zhong, P. Goldner, Emerging rare-earth doped material platforms for quantum nanophotonics, Nanophotonics 8 (2019) 2003–2015.

[16] S. Liu, D. Serrano, A. Fossati, A. Tallaire, A. Ferrier, P. Goldner, Controlled size reduction of rare earth doped nanoparticles for optical quantum technologies, RSC Advances 8 (2018) 37098–37104.

[17] D. Serrano, J. Karlsson, A. Fossati, A. Ferrier, P. Goldner, All-optical control of long-lived nuclear spins in rare-earth doped nanoparticles, Nat. Commun. 9 (2018) 2127.

[18] B. Casabone, J. Benedikter, T. Hummer, F. Oehl, K. d. O. Lima, T. W. Hansch, A. Ferrier, P. Goldner, H. d. Riedmatten, D. Hunger, Cavity-enhanced spectroscopy of a few-ion ensemble in Eu^{3+}:Y_2O_3, New J. Phys. 20 (2018) 095006.

[19] D. Serrano, C. Deshmukh, S. Liu, A. Tallaire, A. Ferrier, H. de Riedmatten, P. Goldner, Coherent optical and spin spectroscopy of nanoscale Pr^{3+}:Y_2O_3, Physical Review B 100 (2019) 144304.

[20] P. Goldner, A. Ferrier, O. Guillot-Noel, Rare earth-doped crystals for quantum information processing, 2015.

[21] S. Liu, A. Fossati, D. Serrano, A. Tallaire, A. Ferrier, P. Goldner, Deffect engineering for quantum grade rare-earth nanocrystals, ACS Nano 14 (2020) 9953.

[22] A. Fossati, S. Liu, J. Karlsson, A. Ikesue, A. Tallaire, A. Ferrier, D. Serrano, P. Goldner, A Frequency-Multiplexed Coherent Electro-optic Memory in Rare Earth Doped Nanoparticles, Nano Letters 20 (2020) 7087–7093. Publisher: American Chemical Society.

[23] J. G. Bartholomew, K. de Oliveira Lima, A. Ferrier, P. Goldner, Optical line width broadening mechanisms at the 10 khz level in Eu^{3+}:Y_2O_3 nanoparticles, Nano Lett. 17 (2017) 778–787.

[24] A. Perrot, P. Goldner, D. Giaume, M. Lovric, C. Andriamiadamanana, R. R. Concalves, A. Ferrier, Narrow optical homogeneous linewidths in rare earth doped nanocrystals, Phys. Rev. Lett. 111 (2013) 203601.

[25] G. K. Liu, R. L. Cone, Laser-induced instantaneous spectral diffusion in Tb^{3+} compounds as observed in photon-echo experiments, Phys. Rev. B 41 (1990) 6193–6200.

[26] W. R. Babbitt, A. Lezama, T. W. Mossberg, Optical dephasing, hyperfine structure, and hyperfine relaxation associated with the 580.8-nm $^7F_0-^5D_0$ transition of europium in Eu^{3+}:Y_2O_3, Phys. Rev. B 39 (1989) 1987–1992.

[27] R. MacFarlane, R. Shelby, Homogeneous line broadening of optical transitions of ions and molecules in glasses, Journal of Luminescence 36 (1987) 179 – 207.

[28] M. Kim, H. Mamin, M. Sherwood, K. Ohno, D. Awschalom, D. Rugar, Decoherence of Near-Surface Nitrogen-Vacancy Centers Due to Electric Field Noise, Physical Review Letters 115 (2015) 087602. Publisher: American Physical Society.

[29] C. W. Thiel, W. R. Babbitt, R. L. Cone, Optical decoherence studies of yttrium oxyorthosilicate Y_2SiO_5 codoped with Er^{3+} and Eu^{3+} for optical signal processing and quantum information applications at 1.5 microns, Phys. Rev. B 85 (2012) 174302.

[30] F. Konz, Y. Sun, C. W. Thiel, R. L. Cone, R. W. Equall, R. L. Hutcheson, R. M. Macfarlane, Temperature and concentration dependence of optical dephasing, spectral-hole lifetime, and anisotropic absorption in Eu:Y_2SiO_5, Phys. Rev. B 68 (2003) 085109.

[31] N. Kunkel, J. Bartholomew, S. Welinski, A. Ferrier, A. Ikesue, P. Goldner, Dephasing mechanisms of optical transitions in rare-earth-doped transparent ceramics, Phys. Rev. B 94 (2016) 184301.

[32] R. Fukumori, Y. Huang, J. Yang, H. Zhang, T. Zhong, Subkilohertz optical homogeneous linewidth and dephasing mechanisms in :Er^{3+}:Y_2O_3 ceramics, Physical Review B 101 (2020) 214202. Publisher: American Physical Society.

[33] N. Kunkel, J. Bartholomew, L. Binet, A. Ikesue, P. Goldner, High-Resolution Optical Line Width Measurements as a Material Characterization Tool, The Journal of Physical Chemistry C 120 (2016) 13725–13731.

[34] N. Kunkel, A. Ferrier, C. W. Thiel, M. O. Ramirez, L. E. Bausa, R. L. Cone, A. Ikesue, P. Goldner, Rare-earth doped transparent ceramics for spectral filtering and quantum information processing, APL Materials 3 (2015) 096103.

[35] G. P. Flinn, K. W. Jang, J. Ganem, M. L. Jones, R. S. Meltzer, R. M. Macfarlane, Sample-dependent optical dephasing in bulk crystalline samples of Y_2O_3:Eu^{3+}, Physical Review B 49 (1994) 5821–5827.

[36] J. X. Zheng, G. Ceder, T. Maxisch, W. K. Chim, W. K. Choi, Native point defects in yttria and relevance to its use as a high-dielectric-constant gate oxide material: First-principles study, Phys. Rev. B 73 (2006) 104101.

[37] B. Lacroix, F. Paumier, R. J. Gaboriaud, Crystal defects and related stress in Y_2O_3 thin films: Origin, modeling, and consequence on the stability of the *C*-type structure, Physical Review B 84 (2011) 014104. Publisher: American Physical Society.

[38] T. Okuno, T. Suemoto, Systematic control of spectral hole burning and homogeneous linewidth by disorder in Y_2O_3:Pr^{3+} crystalline systems, Phys. Rev. B 59 (1999) 9078–9087.